Observation of Dirac Charge Density Waves in Bi_2Te_2Se

Adrian Ruckhofer,[1] Giorgio Benedek,[2,3] Wolfgang E. Ernst,[1] and Anton Tamtögl[1,*]

[1] *Institute of Experimental Physics, Graz University of Technology, Graz, Austria*
[2] *Dipartimento di Scienza dei Materiali, Università degli Studi di Milano-Bicocca, Milano, Italy*
[3] *Donostia International Physics Center, University of the Basque Country, Donostia, San Sebastian, Spain*

While the hexagonal Fermi level contours, often found at the surfaces of topological insulators (TIs) would imply "strong" nesting conditions, the existence of charge density waves (CDWs) - periodic modulations of the electron density - has not been verified up to now. Here, we report the observation of a CDW at the surface of the TI $Bi_2Te_2Se(111)$, below $\approx 350\,K$ by helium atom scattering, and thus experimental evidence of a CDW involving Dirac topological electrons. Deviations of the order parameter observed below 200 K and a low temperature break of time reversal symmetry suggest the onset of a spin density wave with the same period as the CDW in presence of a prominent electron-phonon interaction originating from the Rashba spin-orbit coupling.

Charge density waves (CDWs) - periodic modulations of the electron density - are an ubiquitous phenomenon in crystalline metals and are often observed in layered or low-dimensional materials [1–5]. CDWs are commonly described by a Peierls' transition in a one-dimensional chain of atoms which allows for an opening of an electronic gap at the nesting wavevector causing a Fermi-surface nesting. However, it has been questioned whether the concept of nesting is essential for the understanding of the CDW formation [1, 6]. Instead, CDWs are often driven by strong electronic correlations and wavevector-dependent electron-phonon (e-ph) coupling [7]. Similarly, a nesting of sections of the Fermi surface can induce a periodic spin-density modulation, a spin-density wave (SDW) [8]. The possibility of a simultaneous appearance of both CDW and SDW order has been studied theoretically in earlier works [9], and a SDW was recently predicted for Weyl semimetals [10].

The material class of topological insulators (TIs) has recently attracted extensive attention in a different context [11–16], due to their unique electronic surface states which involve a Dirac cone with spin-momentum locking [17, 18]. Here we report for the first time, experimental evidence for a Dirac CDW on the surface of the TI Bi_2Te_2Se, i.e. a CDW involving Dirac topological electrons. Atom scattering experiments reveal a CDW transition temperature $T_{CDW} = 350\,K$ of the Dirac two-dimensional electron gas (2DEG). The break of time-reversal symmetry of the CDW diffraction peaks observed at low temperature suggests a prominent role of the Rashba spin-orbit coupling with the possible onset of a SDW below 200 K.

Archetypal TIs such as the bismuth chalcogenides share many similarities with common CDW materials such as a layered structure (see Figure 1(a)) [20]. The hexagonal contours at the Fermi level often found in TIs also imply a strong nesting which has led to speculations about the existence of CDWs in TIs. Furthermore, the importance of charge order in the context of unconventional superconductivity in these systems has been subject to recent studies[21, 22]. On the other hand, compared to other CDW materials, the topological surface states (TSS) of

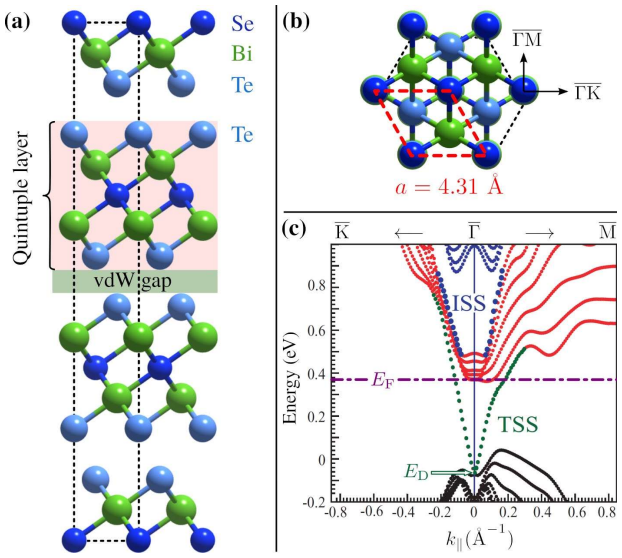

FIG. 1. (a) Side view of the conventional hexagonal unit cell of Bi_2Te_2Se. The unit cell consists of three quintuple layers of which each one is terminated by a Te layer. (b) The (111) cleavage plane of Bi_2Te_2Se with the red rhombus highlighting the hexagonal surface unit cell. (c) Surface band structure of $Bi_2Te_2Se(111)$ calculated by Nurmamat *et al.* [19] (reproduced with permission, copyright 2013 by the American Physical Society) along the symmetry directions $\overline{\Gamma K}$ and $\overline{\Gamma M}$. TSS labels the topological surface states forming the Dirac cone, while internal (quantum-well) surface states (ISS) are also found in the gap above the conduction band minimum. In the present sample the Fermi level E_F (purple dash-dotted line) is located about 0.4 eV above the Dirac point E_D.

TIs such as Bi_2Te_2Se exhibit a characteristic spin polarisation, as studied together with the helical spin texture for the present material in refs. [19, 23].

Among the bismuth chalcogenides, Bi_2Te_2Se is much less studied. Surface dominated electronic transport [24–28] as well as the surface electronic band structure [23, 29–32] have been subject to several investigations. Moreover, in terms of the electronic band structure it was shown that for different $Bi_{2-x}Sb_xTe_{3-y}Se_y$ compositions, the

Dirac point (E_D in Figure 1(c)) moves up in energy with increasing x [29]. Tuning these stoichiometric properties and the doping of materials may give rise to nesting conditions between electron hole/pocket states at the Fermi surface (E_F in Figure 1(c)).

Figure 1(c) depicts the electronic surface band structure calculated by Nurmamat *et al.* [19] along the symmetry directions $\overline{\Gamma K}$ and $\overline{\Gamma M}$ revealing the TSS which form the Dirac cone. The Fermi level E_F (purple line) in our present sample is located about 0.4 eV above the Dirac point yielding the formation of quantum well states at the Fermi surface. Moreover, a near-surface 2DEG with a pronounced spin-orbit splitting can be induced on Bi_2Te_2Se by adsorption of rubidium [33], and surface oxidation may occur at step edge defects after cleaving [34], but Bi_2Te_2Se seems to be less prone to the formation of a 2DEG from rest gas adsorption compared to other TIs [35] as shown in angle resolved photo-emission measurements of the present samples [26]. Dirac fermion dynamics in Bi_2Te_2Se was subject to a recent study by Papalazarou *et al.* [36].

One reason for Bi_2Te_2Se being less studied than the binary bismuth chalcogenides might be the difficulty in synthesising high-quality single crystals, which originates from the internal features of the specific solid-state composition and phase separation in Bi_2Te_2Se [37]. In this work we present a helium atom scattering (HAS) study of Bi_2Te_2Se (phase II of $Bi_2Te_{3-x}Se_x(111)$ with $x \approx 1$[1] and approximated as Bi_2Te_2Se in the following). As helium atoms are scattered off the surface electronic charge distribution, HAS provides access to the surface electron density [38], and is therefore a perfect probe for experimental studies of TIs, since the TSS properties are often mixed up with those of bulk-states [39, 40]. Since the surface electronic transport properties of TIs at finite temperature as well as the appearance of CDWs are influenced by the interaction of electrons with phonons, the e-ph coupling as described in terms of the mass-enhancement factor λ has been subject to several studies [41–45]. For Bi_2Te_2Se it was reported that the electron-disorder interaction dominates scattering processes with $\lambda = 0.12$ [46], in good agreement with the value found from HAS [47].

The experimental data of this work was obtained at a HAS apparatus, where a nearly monochromatic beam of ^{4}He is scattered off the sample surface in a fixed source-sample-detector geometry (for further experimental details see Ref. [48] and supplementary information). The scattered intensity of a He beam in the range of $10 - 20$ meV is then recorded as a function of the incident angle ϑ_i with respect to the surface normal, which can be modified by rotating the sample in the scattering chamber. The momentum transfer parallel to the surface ΔK, upon elastic scattering, is given by $\Delta K = |\mathbf{k}_i| (\sin\vartheta_f - \sin\vartheta_i)$, with $\mathbf{k}_i$, the incident wavevector, and ϑ_i and ϑ_f the incident and final angle, respectively. The Bi_2Te_2Se sample was cleaved *in situ*, in a load-lock chamber [49], prior to the experiments. Due to the weak bonding between the quintuple layers in Figure 1(a), the latter gives access to the (111) cleavage plane with a Te termination at the surface (Figure 1(b)).

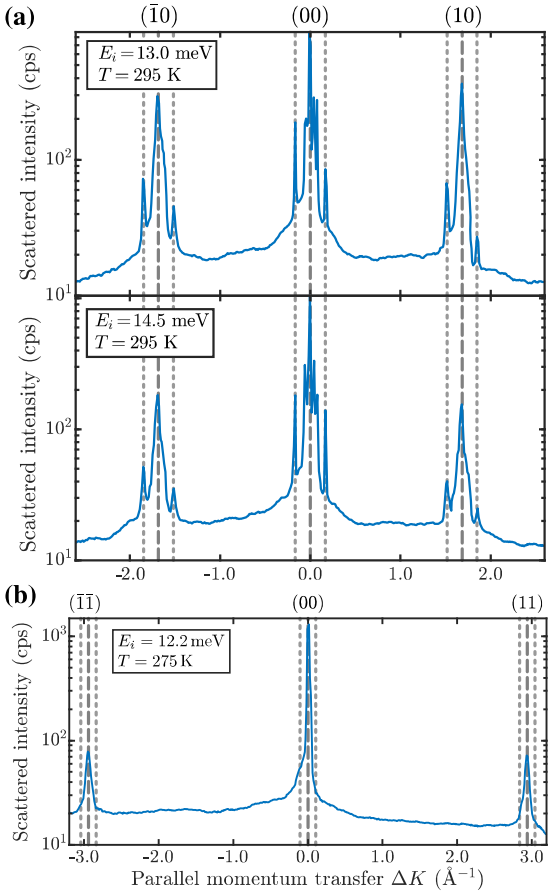

FIG. 2. The CDW periodicity becomes evident in diffraction scans (logarithmic scale) of $Bi_2Te_2Se(111)$. (a) Scans along $\overline{\Gamma M}$ taken at room temperature show satellite peaks (illustrated by the grey dashed vertical lines) next to the specular and first order diffraction peaks (grey dash-dotted vertical lines). (b) Same for the $\overline{\Gamma K}$ direction; in this direction no evident satellite peaks are observed close to the diffraction peaks.

Figure 2 shows the scattered He intensity versus momentum transfer ΔK with the scans taken at different incident beam energies E_i along the $\overline{\Gamma M}$ (a) and $\overline{\Gamma K}$ (b) direction. Along $\overline{\Gamma M}$ there appear sharp additional peaks (illustrated by the vertical dashed lines) next to both the specular and the first order diffraction peaks (vertical dash-dotted lines) at an average spacing of about 0.18 Å^{-1} with respect to the diffraction peaks (Figure 2 and Figure 3(b) in an enlarged scale). The fact that these satellite peaks appear at the same momentum transfer

[1] According to the surface lattice constant $a = 4.31$ Å as determined by HAS and Fig. 1(b) of [37], $x \approx 1$ for the present sample.

$\Delta K \approx \pm 0.18$ Å^{-1} with respect to the specular as well as to the first order diffraction peaks, independently of the incident energy, shows that they cannot be caused by bound-state resonances [50], but have to be necessarily ascribed to a long-period surface superstructure of the electron density, i.e., a surface CDW. In addition, due to the position of the peaks and the later described temperature dependence these features can not be attributed to any superstructure formed by adsorbates at the surface.

For a triangular set of electron pockets with the same spin at the Fermi level, each one located at a distance k_F from the zone centre, the inter-pocket nesting gives rise to satellite peaks at $\Delta K = \frac{3}{2}k_F$ in the $\overline{\Gamma M}$ direction and $\frac{\sqrt{3}}{2}k_F$ in the $\overline{\Gamma K}$ direction. The CDW diffraction peaks are, however, observed only in the $\overline{\Gamma M}$ direction, and give $k_F = 0.12$ Å^{-1}. Our HAS data is best compared with differential conductance (DC) maps since from the latter, experimental values of the nesting vectors can be extracted. Scattering measurements obtained in momentum space can then be directly compared with the Fourier transform of scanning tunnelling microscopy (STM) DC maps in reciprocal space. Figure 3 shows the consistency between a measured DC map by Nurmamat *et al.* [19] and an angular diffraction scan. The DC map depicts that for the Fermi level above the conduction band minimum the hexagonal Fermi contour and the corresponding DC map evolve to a hexastar, here reproduced in Figure 3(a) with a slight change of the wavevector scale (corresponding to a DC bias of 0.36 eV) so as to adapt it to the experimental nesting wavevector. Room temperature data (red curve in Figure 3(b)) directly reflects the symmetrised DC map, with the low temperature disappearance of the $+\mathbf{g}_{\mathrm{CDW}}$ peak as explained below. The complex satellite structure next to the specular peak is in close correspondence with the large intensity at the center of the DC map, associated with the surface quantum well states at the bottom of the conduction band. Similarly to surface resistance, which is caused by electron scattering processes at the Fermi level, in HAS diffraction from a CDW, a wavevector $\mathbf{g}_{\mathrm{CDW}}$ is transferred to the surface electron gas via a Fermi-level electron-hole pair excitation. Both processes are enhanced by good nesting conditions, showing peaks at the same position in reciprocal space. In both cases these processes are quasi-elastic, especially at low temperature and in presence of a small CDW gap at the Fermi level.

In the following, we consider the temperature dependence of the CDW diffraction peaks and the CDW critical temperature T_{CDW}. Upon measuring the scattered intensities as a function of surface temperature it turns out that the intensity of the satellite peaks decreases much faster than the intensity of the specular peak. As shown in the supplementary information Figure S1, when plotting both peaks in a Debye-Waller plot, the slope of the satellite peak is clearly steeper than the one of the specular peak.

Based on the theory of classical CDW systems, the square root of the integrated peak intensity can be viewed as the order parameter of a CDW [51, 52]. Figure 4 shows the temperature dependence of the square root of the integrated intensity for the $-\mathbf{g}_{\mathrm{CDW}}$ peak on the left-hand side of the specular peak (inset of Figure 4). In order to access the intensity change relevant to the CDW system as opposed to the intensity changes due to the Debye-Waller factor, the integrated intensity $I(T)$ has been normalised to that of the specular beam [50] - a correction which is necessary in view of the low surface Debye temperature of $Bi_2Te_2Se(111)$ [47]. The temperature dependence of

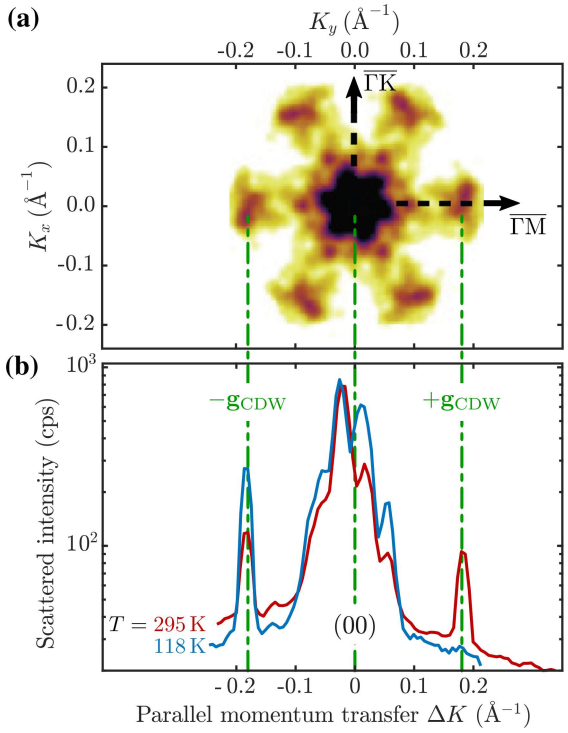

FIG. 3. The nesting condition giving rise to the CDW satellite peaks around the (00)-reflection is confirmed by Fourier transformed differential conductance (DC) maps. The hexagonally-symmetrised map of $Bi_2Te_2Se(111)$ by Nurmamat *et al.* [19] (reproduced with permission, copyright 2013 by the American Physical Society) at 0.36 eV above the Dirac point in (a), is in excellent agreement with the satellite structure around the specular peak of $Bi_2Te_2Se(111)$ measured with HAS in the $\overline{\Gamma M}$ direction at room temperature (295 K) and plotted as red line in (b). The nestings in the $\overline{\Gamma K}$ direction, on the other hand, imply spin reversal and no CDW satellite peaks are detected by HAS in that direction (see Figure 2(b)). The sharp peaks close to $+\mathbf{g}_{\mathrm{CDW}}$ are assigned to a CDW, while the missing CDW peak at low temperature (118 K, blue line) on the right-hand side is attributed to the Rashba effect after the onset of a SDW spin ordering. Since the hexagonal symmetrisation of the DC map in (a) removes the effect of possible time-reversal symmetry breaking, the comparison is to be made with the room temperature HAS diffraction scan in (b). The complex structure aside the specular peak can be associated with transitions involving surface quantum-well states (see Figure 1(c) and Figure 2(a)).

the order parameter $\sqrt{I(T)}$ can be used to determine the CDW transition temperature T_{CDW} and the critical exponent β belonging to the phase transition by fitting the power law

$$\sqrt{\frac{I(T)}{I(0)}} = \left(1 - \frac{T}{T_{CDW}}\right)^{\beta} , \qquad (1)$$

to the data points in Figure 4. Here, $I(0)$ is the extrapolated intensity at 0 K. The fit is represented by the green dashed line in Figure 4, resulting in $T_{CDW} = (350 \pm 10)$K and $\beta = (0.34 \pm 0.02)$.

The exact peak position and width of the satellite peak was determined by fitting a single Gaussian to the experimental data. The inset of Figure 4 shows a shift of the satellite peak position to the right with increasing surface temperature, i.e. $\mathbf{g}_{\mathrm{CDW}}$ decreases with increasing temperature, as illustrated by the grey line. Such a temperature dependence confirms the connection of the satellite peaks with the surface electronic structure. A shift of the Dirac point to lower binding energies with increasing temperature and thus a decrease of k_F has been observed both for Bi_2Te_2Se(111) [53] as well as for Bi_2Se_3(111) [54]. As reported by Nayak *et al.* [53], the temperature dependent changes of the electronic structure at E_F occur due to the shift of the chemical potential in the case of n-type Bi_2Te_2Se(111). Moreover, a strong temperature dependence of the chemical potential has also been observed for other CDW systems [55] and semiconductors [56].

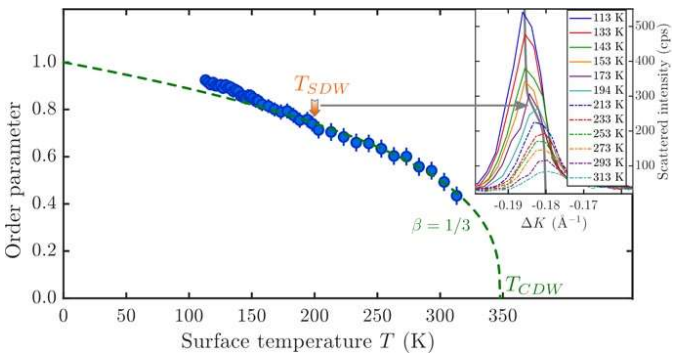

FIG. 4. Order parameter of the surface CDW (blue circles), as extracted from the temperature dependence of the $-\mathbf{g}_{\mathrm{CDW}}$ CDW peak intensity of Figure 3(b) (see text). The fit with the fluctuation critical exponent $\beta = 1/3$ [57] (green dashed line) yields a critical temperature T_{CDW} of about 350 K. The inset shows a rapid shift of the satellite peak, occurring at around 200 K, from a momentum transfer of 0.18 Å^{-1} to 0.186 Å^{-1}. Together with the corresponding deviation of the order-parameter fit below about 200 K (T_{SDW}) and the time-reversal symmetry break (missing $+\mathbf{g}_{\mathrm{CDW}}$ peak at low T in Figure 3(b)), it suggests the onset of a spin ordering (a spin-density wave), which allows, through the Rashba effect, for a parallel momentum transfer only in one direction.

The surprising disappearance of the $+\mathbf{g}_{\mathrm{CDW}}$ diffraction peak observed at low temperature (118 K) is likely to be related to the apparent phase transition occurring at about 200 K (illustrated by the arrow in Figure 4), possibly a spin ordering within the CDW, i.e., a SDW with the same period. The latter is indicated by a rapid shift of the $-\mathbf{g}_{\mathrm{CDW}}$ diffraction peak position around 200 K, corresponding to a slight contraction of the CDW period (inset of Figure 4). The CDW order parameter, expressed by $(1 - T/T_{CDW})^{\beta}$ actually shows a small deviation from this law below about 200 K (T_{SDW} in Figure 4). As explained above, the He-atom diffraction process from the CDW occurs via parallel momentum transfer to the surface electron gas, via an electron-hole excitation between a filled and an empty state of equal spin and well nested at the Fermi level. Thus, the unidirectionality of the process at low temperature suggests a prominent role of the Rashba term in presence of spin ordering and strong implications for the e-ph contribution.

The latter is in line with Guan *et al.* [58], who reported a large enhancement of the e-ph coupling in the Rashba-split state of the Bi/Ag(111) surface alloy. The larger overlap of He atoms with CDW maxima also selects electrons with the same spin, because the SDW and CDW exhibit the same period. Considering in the present case a free-electron Hamiltonian [59],

$$-E_{\mathrm{D}} + \left(\frac{\mathbf{p}^2}{2m^*}\right) + \alpha_R\, \boldsymbol{\sigma} \cdot (\mathbf{p} \times \hat{\mathbf{z}}) ,$$

where $-E_{\mathrm{D}}$ is the energy of the Dirac point below the Fermi energy $E_{\mathrm{F}} = 0$, $\mathbf{p}$ the surface electron momentum, and m^* its effective mass, $\boldsymbol{\sigma}$ the spin operator, $\hat{\mathbf{z}}$ the unit vector normal to the surface and α_R the Rashba constant. The modulation of the Rashba term

$$\frac{\partial \alpha_R}{\partial A_{\mathbf{q}s}}\, A_{\mathbf{q}s}\, \boldsymbol{\sigma} \cdot (\mathbf{q} \times \hat{\mathbf{z}}) ,$$

produced by a phonon of momentum $\mathbf{q}$, branch index s and normal mode coordinate $A_{\mathbf{q}s}$ is viewed as the main source of e-ph interaction [60], causing interpocket coupling ($\Delta\mathbf{p} = \mathbf{q} = \pm\mathbf{g}_{\mathrm{CDW}}$) and the CDW gap opening.

In a diffraction process the exchange of parallel momentum between the scattered atom and the solid centre-of-mass is mediated by a virtual electron interpocket transition $|\mathbf{k}, n\rangle \rightarrow |\mathbf{k} + \mathbf{q}, n'\rangle$ weighed by the difference in Fermi-Dirac occupation numbers $f_{\mathbf{q},n} - f_{\mathbf{k}+\mathbf{q},n'}$. While the process $\mathbf{q} = -\mathbf{g}_{\mathrm{CDW}}$ virtually casts the electron from a pocket ground state at the Fermi level to an empty excited state across that gap, the process $\mathbf{q} = +\mathbf{g}_{\mathrm{CDW}}$ would virtually send the electron, because of the Rashba term, to a lower energy state and is therefore forbidden at low temperature.

Such a scenario is equivalent to saying that the SDW-CDW entanglement makes HAS sensitive to the spin orientation via its temperature dependence. The interpocket electron transition across the gap accompanying a CDW diffraction of He atoms via the

modulation of the Rashba term may only occur in one direction. Since the gap energy is of the order of room temperature and at this temperature the spin ordering is removed, the above selection rule is relaxed and the diffraction peaks are observed in both directions (on both sides of the specular in Figure 3(b)). The interpretation of the missing diffraction peak at low temperature, cannot be tested based on existing STM data [19], since they have been reported after hexagonal symmetrisation. The corresponding time-reversal symmetry break should, however, actually be reflected in as-measured DC maps at low temperature.

In summary, we have provided evidence by means of helium atom scattering, of a surface charge density wave in $Bi_2Te_2Se(111)$ occurring below 345 K and involving Dirac topological electrons. The CDW diffraction pattern is found to closely reflect the nesting condition of previously reported differential conductance maps for a Fermi level 370 meV above the Dirac point [19]. The CDW order parameter has been measured down to 108 K and found to have a critical exponent of 1/3. The observation of a time-reversal symmetry break at low temperature, together with deviations from the critical behaviour below about 200 K, are interpreted as due to the onset of a spin density wave with the same period as the CDW in presence of a prominent electron-phonon interaction originating from the Rashba spin-orbit coupling.
While it is difficult to make definitive statements about the generality of our observations, we anticipate that by tuning the stoichiometric properties and doping level of topological insulators - thus changing the position of the Dirac point and possible nesting conditions - the condition for CDW order may be changed or shifted to a different periodicity. It is thus expected that from further experiments and validation one may be able to evolve phase diagrams for Dirac CDWs as a function of stoichiometry, doping and Fermi level position. Taken together the results promise also to shed light on previous experimental and theoretical investigations of related systems and how CDW order affects lattice dynamics and stability.

The authors gratefully acknowledge support by the FWF within the projects J3479-N20, P29641-N36 and P34704. We thank Martin Bremholm for the synthesis of the samples, Marco Bianchi for his advice and help in terms of the sample preparation, and Philip Hofmann as well as the aforementioned colleagues for useful discussions and additional characterisations of the samples. We would also like to thank Evgueni Chulkov (DIPC, San Sebastian, Spain) and D. Campi & M. Bernasconi (Unimib, Milano, Italy) for many helpful discussions

* tamtoegl@gmail.com

[1] D. S. Inosov, V. B. Zabolotnyy, D. V. Evtushinsky, A. A. Kordyuk, B. Büchner, R. Follath, H. Berger, and S. V. Borisenko, Fermi surface nesting in several transition metal dichalcogenides, New J. Phys. **10**, 125027 (2008).
[2] F. Arnold, A. Isidori, E. Kampert, B. Yager, M. Eschrig, and J. Saunders, Charge density waves in graphite: Towards the magnetic ultraquantum limit, Phys. Rev. Lett. **119**, 136601 (2017).
[3] J. Hall, N. Ehlen, J. Berges, E. van Loon, C. van Efferen, C. Murray, M. Rösner, J. Li, B. V. Senkovskiy, M. Hell, M. Rolf, T. Heider, M. C. Asensio, J. Avila, L. Plucinski, T. Wehling, A. Grüneis, and T. Michely, Environmental Control of Charge Density Wave Order in Monolayer 2H-TaS_2, ACS Nano **13**, 10210 (2019).
[4] S.-Z. Wang, Y.-M. Zhang, J.-Q. Fan, M.-Q. Ren, C.-L. Song, X.-C. Ma, and Q.-K. Xue, Charge density waves and Fermi level pinning in monolayer and bilayer $SnSe_2$, Phys. Rev. B **102**, 241408 (2020).
[5] W. Shi, B. J. Wieder, H. L. Meyerheim, Y. Sun, Y. Zhang, Y. Li, L. Shen, Y. Qi, L. Yang, J. Jena, P. Werner, K. Koepernik, S. Parkin, Y. Chen, C. Felser, B. A. Bernevig, and Z. Wang, A charge-density-wave topological semimetal, Nat. Phys. **17**, 381 (2021).
[6] M. D. Johannes and I. I. Mazin, Fermi surface nesting and the origin of charge density waves in metals, Phys. Rev. B **77**, 165135 (2008).
[7] K. Rossnagel, On the origin of charge-density waves in select layered transition-metal dichalcogenides, J. Phys.: Condens. Matter **23**, 213001 (2011).
[8] A. M. Gabovich, A. I. Voitenko, J. F. Annett, and M. Ausloos, Charge- and spin-density-wave superconductors, Superconductor Science and Technology **14**, R1 (2001).
[9] R. S. Fishman and S. H. Liu, Effect of impurities on the magnetic ordering in chromium, Phys. Rev. B **45**, 12306 (1992).
[10] S. Kundu and D. Sénéchal, Spin density wave order in interacting type-I and type-II Weyl semimetals, Phys. Rev. B **103**, 085136 (2021).
[11] B. Bradlyn, L. Elcoro, J. Cano, M. G. Vergniory, Z. Wang, C. Felser, M. I. Aroyo, and B. A. Bernevig, Topological quantum chemistry, Nature **547**, 298 (2017).
[12] A. Bansil, H. Lin, and T. Das, Colloquium: Topological band theory, Rev. Mod. Phys. **88**, 021004 (2016).
[13] M. Z. Hasan, S.-Y. Xu, and G. Bian, Topological insulators, topological superconductors and Weyl fermion semimetals: discoveries, perspectives and outlooks, Phys. Scr. **T164**, 014001 (2015).
[14] Y. Ando, Topological Insulator Materials, J. Phys. Soc. Jpn. **82**, 102001 (2013).
[15] X.-L. Qi and S.-C. Zhang, Topological insulators and superconductors, Rev. Mod. Phys. **83**, 1057 (2011).
[16] M. Z. Hasan and C. L. Kane, Colloquium: Topological insulators, Rev. Mod. Phys. **82**, 3045 (2010).
[17] J. E. Moore, The birth of topological insulators, Nature **464**, 194 (2010).
[18] Y. L. Chen, J. G. Analytis, J.-H. Chu, Z. K. Liu, S.-K. Mo, X. L. Qi, H. J. Zhang, D. H. Lu, X. Dai, Z. Fang, S. C. Zhang, I. R. Fisher, Z. Hussain, and Z.-X. Shen, Experimental Realization of a Three-Dimensional Topological Insulator, Bi_2Te_3, Science **325**, 178 (2009).
[19] M. Nurmamat, E. E. Krasovskii, K. Kuroda, M. Ye, K. Miyamoto, M. Nakatake, T. Okuda, H. Namatame, M. Taniguchi, E. V. Chulkov, K. A. Kokh, O. E. Tereshchenko, and A. Kimura, Unoccupied topological

surface state in Bi_2Te_2Se, Phys. Rev. B **88**, 081301 (2013).
[20] A. Tamtögl, D. Campi, M. Bremholm, E. M. J. Hedegaard, B. B. Iversen, M. Bianchi, P. Hofmann, N. Marzari, G. Benedek, J. Ellis, and W. Allison, Nanoscale Surface Dynamics of Bi_2Te_3(111): Observation of a Prominent Surface Acoustic Wave and the Role of van der Waals Interactions, Nanoscale **10**, 14627 (2018).
[21] B. J. Lawson, P. Corbae, G. Li, F. Yu, T. Asaba, C. Tinsman, Y. Qiu, J. E. Medvedeva, Y. S. Hor, and L. Li, Multiple Fermi surfaces in superconducting Nb-doped Bi_2Se_3, Phys. Rev. B **94**, 041114 (2016).
[22] S. M. Kevy, H. E. Lund, L. Wollesen, K. J. Dalgaard, Y.-T. Hsu, S. Wiedmann, M. Bianchi, A. J. U. Holt, D. Curcio, D. Biswas, A. J. H. Jones, K. Volckaert, C. Cacho, P. Dudin, P. Hofmann, and M. Bremholm, Structural and electronic inhomogeneity of superconducting Nb-doped Bi_2Se_3, Phys. Rev. B **103**, 085107 (2021).
[23] K. Miyamoto, A. Kimura, T. Okuda, H. Miyahara, K. Kuroda, H. Namatame, M. Taniguchi, S. V. Eremeev, T. V. Menshchikova, E. V. Chulkov, K. A. Kokh, and O. E. Tereshchenko, Topological Surface States with Persistent High Spin Polarization across the Dirac Point in Bi_2Te_2Se and Bi_2Se_2Te, Phys. Rev. Lett. **109**, 166802 (2012).
[24] Z. Ren, A. A. Taskin, S. Sasaki, K. Segawa, and Y. Ando, Large bulk resistivity and surface quantum oscillations in the topological insulator Bi_2Te_2Se, Phys. Rev. B **82**, 241306 (2010).
[25] P. Gehring, B. F. Gao, M. Burghard, and K. Kern, Growth of High-Mobility Bi_2Te_2Se Nanoplatelets on hBN Sheets by van der Waals Epitaxy, Nano Lett. **12**, 5137 (2012).
[26] L. Barreto, L. Kühnemund, F. Edler, C. Tegenkamp, J. Mi, M. Bremholm, B. B. Iversen, C. Frydendahl, M. Bianchi, and P. Hofmann, Surface-Dominated Transport on a Bulk Topological Insulator, Nano Lett. **14**, 3755 (2014).
[27] C. Shekhar, C. E. ViolBarbosa, B. Yan, S. Ouardi, W. Schnelle, G. H. Fecher, and C. Felser, Evidence of surface transport and weak antilocalization in a single crystal of the Bi_2Te_2Se topological insulator, Phys. Rev. B **90**, 165140 (2014).
[28] H. Cao, C. Liu, J. Tian, Y. Xu, I. Miotkowski, M. Z. Hasan, and Y. P. Chen, Controlling and distinguishing electronic transport of topological and trivial surface states in a topological insulator (2014), arXiv:1409.3217 [cond-mat.mtrl-sci].
[29] T. Arakane, T. Sato, S. Souma, K. Kosaka, K. Nakayama, M. Komatsu, T. Takahashi, Z. Ren, K. Segawa, and Y. Ando, Tunable Dirac cone in the topological insulator $Bi_{2-x}Sb_xTe3 - ySe_y$, Nat. Commun. **3**, 636 (2012).
[30] M. Neupane, S.-Y. Xu, L. A. Wray, A. Petersen, R. Shankar, N. Alidoust, C. Liu, A. Fedorov, H. Ji, J. M. Allred, Y. S. Hor, T.-R. Chang, H.-T. Jeng, H. Lin, A. Bansil, R. J. Cava, and M. Z. Hasan, Topological surface states and dirac point tuning in ternary topological insulators, Phys. Rev. B **85**, 235406 (2012).
[31] H. Maaß, S. Schreyeck, S. Schatz, S. Fiedler, C. Seibel, P. Lutz, G. Karczewski, H. Bentmann, C. Gould, K. Brunner, L. W. Molenkamp, and F. Reinert, Electronic structure and morphology of epitaxial Bi_2Te_2Se topological insulator films, J. Appl. Phys. **116**, 193708 (2014).
[32] E. Frantzeskakis, N. de Jong, B. Zwartsenberg, T. V. Bay, Y. K. Huang, S. V. Ramankutty, A. Tytarenko, D. Wu, Y. Pan, S. Hollanders, M. Radovic, N. C. Plumb, N. Xu, M. Shi, C. Lupulescu, T. Arion, R. Ovsyannikov, A. Varykhalov, W. Eberhardt, A. de Visser, E. van Heumen, and M. S. Golden, Dirac states with knobs on: Interplay of external parameters and the surface electronic properties of three-dimensional topological insulators, Phys. Rev. B **91**, 205134 (2015).
[33] M. Michiardi, M. Bianchi, M. Dendzik, J. A. Miwa, M. Hoesch, T. K. Kim, P. Matzen, J. Mi, M. Bremholm, B. B. Iversen, and P. Hofmann, Strongly anisotropic spin-orbit splitting in a two-dimensional electron gas, Phys. Rev. B **91**, 035445 (2015).
[34] C. R. Thomas, M. K. Vallon, M. G. Frith, H. Sezen, S. K. Kushwaha, R. J. Cava, J. Schwartz, and S. L. Bernasek, Surface Oxidation of $Bi_2(Te,Se)_3$ Topological Insulators Depends on Cleavage Accuracy, Chem. Mater. **28**, 35 (2016).
[35] E. Frantzeskakis, S. V. Ramankutty, N. de Jong, Y. K. Huang, Y. Pan, A. Tytarenko, M. Radovic, N. C. Plumb, M. Shi, A. Varykhalov, A. de Visser, E. van Heumen, and M. S. Golden, Trigger of the ubiquitous surface band bending in 3D topological insulators, Phys. Rev. X **7**, 041041 (2017).
[36] E. Papalazarou, L. Khalil, M. Caputo, L. Perfetti, N. Nilforoushan, H. Deng, Z. Chen, S. Zhao, A. Taleb-Ibrahimi, M. Konczykowski, A. Hruban, A. Wołoś, A. Materna, L. Krusin-Elbaum, and M. Marsi, Unraveling the Dirac fermion dynamics of the bulk-insulating topological system Bi_2Te_2Se, Phys. Rev. Materials **2**, 104202 (2018).
[37] J.-L. Mi, M. Bremholm, M. Bianchi, K. Borup, S. Johnsen, M. Søndergaard, D. Guan, R. C. Hatch, P. Hofmann, and B. B. Iversen, Phase separation and bulk p-n transition in single crystals of Bi_2Te_2Se topological insulator, Adv. Mater **25**, 889 (2013).
[38] A. Tamtögl, P. Kraus, M. Mayrhofer-Reinhartshuber, G. Benedek, M. Bernasconi, D. Dragoni, D. Campi, and W. E. Ernst, Statics and dynamics of multivalley charge density waves in Sb(111), npj Quantum Mater. **4**, 28 (2019).
[39] L. Viti, D. Coquillat, A. Politano, K. A. Kokh, Z. S. Aliev, M. B. Babanly, O. E. Tereshchenko, W. Knap, E. V. Chulkov, and M. S. Vitiello, Plasma-wave terahertz detection mediated by topological insulators surface states, Nano Lett. **16**, 80 (2016).
[40] T. Knispel, W. Jolie, N. Borgwardt, J. Lux, Z. Wang, Y. Ando, A. Rosch, T. Michely, and M. Grüninger, Charge puddles in the bulk and on the surface of the topological insulator $BiSbTeSe_2$ studied by scanning tunneling microscopy and optical spectroscopy, Phys. Rev. B **96**, 195135 (2017).
[41] R. C. Hatch, M. Bianchi, D. Guan, S. Bao, J. Mi, B. B. Iversen, L. Nilsson, L. Hornekær, and P. Hofmann, Stability of the Bi_2Se_3(111) topological state: Electron-phonon and electron-defect scattering, Phys. Rev. B **83**, 241303 (2011).
[42] J. A. Sobota, S.-L. Yang, D. Leuenberger, A. F. Kemper, J. G. Analytis, I. R. Fisher, P. S. Kirchmann, T. P. Devereaux, and Z.-X. Shen, Distinguishing bulk and surface electron-phonon coupling in the topological insulator Bi_2Se_3 using time-resolved photoemission spectroscopy, Phys. Rev. Lett. **113**, 157401 (2014).
[43] R. Heid, I. Y. Sklyadneva, and E. V. Chulkov, Electron-phonon coupling in topological surface states: The role of polar optical modes, Sci. Rep. **7**, 1095 (2017).
[44] A. Tamtögl, P. Kraus, N. Avidor, M. Bremholm, E. M. J. Hedegaard, B. B. Iversen, M. Bianchi, P. Hofmann,

J. Ellis, W. Allison, G. Benedek, and W. E. Ernst, Electron-phonon coupling and surface Debye temperature of $Bi_2Te_3(111)$ from helium atom scattering, Phys. Rev. B **95**, 195401 (2017).

[45] C. In, S. Sim, B. Kim, H. Bae, H. Jung, W. Jang, M. Son, J. Moon, M. Salehi, S. Y. Seo, A. Soon, M.-H. Ham, H. Lee, S. Oh, D. Kim, M.-H. Jo, and H. Choi, Control over electron-phonon interaction by dirac plasmon engineering in the Bi_2Se_3 topological insulato, Nano Lett. **18**, 734 (2018).

[46] C. Chen, Z. Xie, Y. Feng, H. Yi, A. Liang, S. He, D. Mou, J. He, Y. Peng, X. Liu, *et al.*, Tunable Dirac fermion dynamics in topological insulators, Sci. Rep. **3**, 2411 (2013).

[47] G. Benedek, S. Miret-Artés, J. R. Manson, A. Ruckhofer, W. E. Ernst, and A. Tamtögl, Origin of the electron-phonon interaction of topological semimetal surfaces measured with helium atom scattering, J. Phys. Chem. Lett. **11**, 1927 (2020).

[48] A. Tamtögl, M. Mayrhofer-Reinhartshuber, N. Balak, W. E. Ernst, and K. H. Rieder, Elastic and inelastic scattering of He atoms from Bi(111), J. Phys.: Condens. Matter **22**, 304019 (2010).

[49] A. Tamtögl, E. A. Carter, D. J. Ward, N. Avidor, P. R. Kole, A. P. Jardine, J. Ellis, and W. Allison, Note: A simple sample transfer alignment for ultra-high vacuum systems, Rev. Sci. Instrum. **87**, 066108 (2016).

[50] P. Hofmann, M. M. Ugeda, A. Tamtögl, A. Ruckhofer, W. E. Ernst, G. Benedek, A. J. Martínez-Galera, A. Stróżecka, J. M. Gómez-Rodríguez, E. Rienks, M. F. Jensen, J. I. Pascual, and J. W. Wells, Strong-coupling charge density wave in a one-dimensional topological metal, Phys. Rev. B **99**, 035438 (2019).

[51] G. Grüner, *Density waves in solids*, Frontiers in physics, Vol. 89 (Perseus Publishing, Cambridge, Massachusetts, 1994).

[52] G. Grüner, The dynamics of charge-density waves, Rev. Mod. Phys. **60**, 1129 (1988).

[53] J. Nayak, G. H. Fecher, S. Ouardi, C. Shekhar, C. Tusche, S. Ueda, E. Ikenaga, and C. Felser, Temperature-induced modification of the Dirac cone in the tetradymite topological insulator Bi_2Te_2Se, Phys. Rev. B **98**, 075206 (2018).

[54] Z.-H. Pan, A. V. Fedorov, D. Gardner, Y. S. Lee, S. Chu, and T. Valla, Measurement of an exceptionally weak electron-phonon coupling on the surface of the topological insulator Bi_2Se_3 using angle-resolved photoemission spectroscopy, Phys. Rev. Lett. **108**, 187001 (2012).

[55] C. Monney, E. F. Schwier, M. G. Garnier, N. Mariotti, C. Didiot, H. Beck, P. Aebi, H. Cercellier, J. Marcus, C. Battaglia, H. Berger, and A. N. Titov, Temperature-dependent photoemission on 1T-$TiSe_2$: Interpretation within the exciton condensate phase model, Phys. Rev. B **81**, 155104 (2010).

[56] K. Fukutani, T. Sato, P. V. Galiy, K. Sugawara, and T. Takahashi, Tunable two-dimensional electron gas at the surface of thermoelectric material In_4Se_3, Phys. Rev. B **93**, 205156 (2016).

[57] R. Liu, T. Ma, S. Wang, and J. Yang, Dynamic theory of fluctuations and ciritcal exponents of thermodynamic phase transitions (2019), working paper or preprint.

[58] D. Guan, M. Bianchi, S. Bao, E. Perkins, F. Meier, J. H. Dil, J. Osterwalder, and P. Hofmann, Strongly enhanced electron-phonon coupling in the rashba-split state of the Bi/Ag(111) surface alloy, Phys. Rev. B **83**, 155451 (2011).

[59] P. C. Verpoort and V. Narayan, Chirality relaxation in low-temperature strongly rashba-coupled systems, J. Phys.: Condens. Matter **32**, 355704 (2020).

[60] B. S. Kandemir and D. Akay, The effect of electron-phonon coupling in spin–orbit-coupled graphene, Philos. Mag. **97**, 2225 (2017).

SUPPLEMENTARY INFORMATION: OBSERVATION OF DIRAC CHARGE DENSITY WAVES IN BI_2TE_2SE

EXPERIMENTAL DETAILS

The experimental data of this work were obtained at the HAS apparatus in Graz, where a nearly monochromatic beam of ^{4}He is scattered off the sample surface in a fixed source-sample-detector geometry with an angle of 91.5° (for further details about the apparatus see Ref. [48]). The scattered intensity of a He beam in the range of $10 - 20$ meV is then monitored as a function of the incident angle ϑ_i with respect to the surface normal, which can be modified by rotating the sample in the main chamber (base pressure $p \leq 2 \cdot 10^{-10}$ mbar). The momentum transfer parallel to the surface ΔK, upon elastic scattering, is given by $\Delta K = |\mathbf{k}_i| (\sin \vartheta_f - \sin \vartheta_i)$, with $\mathbf{k}_i$, the incident wavevector, and ϑ_i and ϑ_f the incident and final angle, respectively.

The Bi_2Te_2Se sample was fixed on a sample holder using thermally and electrically conductive epoxy and cleaved *in situ*, in a load-lock chamber [49]. The sample temperature can be varied by cooling via a thermal connection to a liquid nitrogen reservoir and heating based on a button heater. After cleavage, the cleanness and purity of the sample can be further checked using low energy electron diffraction (LEED) and Auger electron spectroscopy (AES). Details about the sample growth procedure can be found in Mi *et al.* [37]. Bi_2Te_2Se exhibits a rhombohedral crystal structure, which is in accordance with other bismuth chalcogenides built of quintuple layers (QL, see Figure 1 in main text) which are bound to each other via weak forces of van der Waals character [37]. The conventional hexagonal unit cell consists of 3 QLs with each QL layer being terminated by a Te layer (Figure 1(a) in main text). The weak bonding between the QLs gives access to the (111) cleavage plane with the described Te termination and a surface lattice constant of $a = 4.31$ Å (Figure 1(b) in main text).

ANOMALOUS DEBYE ATTENUATION

Figure S1 shows the obtained temperature dependence of the diffraction intensities of the specular reflection (blue) and the satellite peak (red) which forms the basis for interpretation of the CDW formation. The data plotted in Figure S1 is applied for the derivation of the order parameter in Figure 4 in the main text.

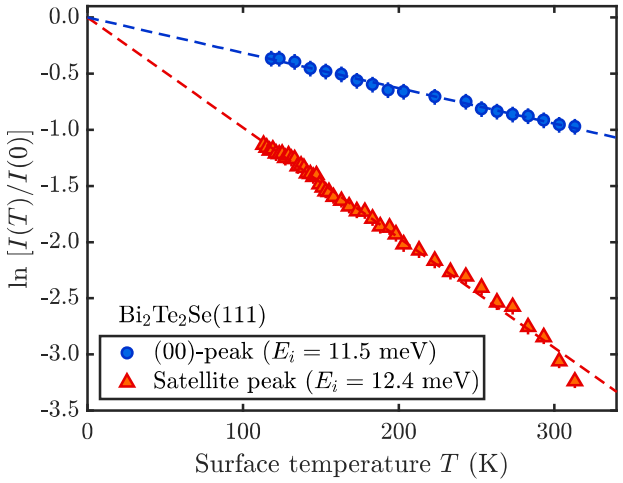

FIG. S1. Debye-Waller plot of the temperature dependence for both the specular as well as the satellite peak at the left hand side of the specular peak.